

# A bimodular mechanism of calcium control in eukaryotes

Henning Tidow<sup>1,2\*</sup>, Lisbeth R. Poulsen<sup>1,3\*</sup>, Antonina Andreeva<sup>4</sup>, Michael Knudsen<sup>1,5</sup>, Kim L. Hein<sup>1,2†</sup>, Carsten Wiuf<sup>6</sup>, Michael G. Palmgren<sup>1,3</sup> & Poul Nissen<sup>1,2</sup>

Calcium ions ( $\text{Ca}^{2+}$ ) have an important role as secondary messengers in numerous signal transduction processes<sup>1–4</sup>, and cells invest much energy in controlling and maintaining a steep gradient between intracellular ( $\sim 0.1$ -micromolar) and extracellular ( $\sim 2$ -millimolar)  $\text{Ca}^{2+}$  concentrations<sup>1</sup>. Calmodulin-stimulated calcium pumps, which include the plasma-membrane  $\text{Ca}^{2+}$ -ATPases (PMCA), are key regulators of intracellular  $\text{Ca}^{2+}$  in eukaryotes<sup>5–8</sup>. They contain a unique amino- or carboxy-terminal regulatory domain responsible for autoinhibition, and binding of calcium-loaded calmodulin to this domain releases autoinhibition and activates the pump. However, the structural basis for the activation mechanism is unknown and a key remaining question is how calmodulin-mediated PMCA regulation can cover both basal  $\text{Ca}^{2+}$  levels in the nanomolar range as well as micromolar-range  $\text{Ca}^{2+}$  transients generated by cell stimulation<sup>7</sup>. Here we present an integrated study combining the determination of the high-resolution crystal structure of a PMCA regulatory-domain/calmodulin complex with *in vivo* characterization and biochemical, biophysical and bioinformatics data that provide mechanistic insights into a two-step PMCA activation mechanism mediated by calcium-loaded calmodulin. The structure shows the entire PMCA regulatory domain and reveals an unexpected 2:1 stoichiometry with two calcium-loaded calmodulin molecules binding to different sites on a long helix. A multifaceted characterization of the role of both sites leads to a general structural model for calmodulin-mediated regulation of PMCA that allows stringent, highly responsive control of intracellular calcium in eukaryotes, making it possible to maintain a stable, basal level at a threshold  $\text{Ca}^{2+}$  concentration, where steep activation occurs.

Compared with other P-type ATPases, calmodulin-stimulated calcium pumps contain an additional autoinhibitory or regulatory (R) domain at the N terminus<sup>9</sup> (in plants) or C terminus<sup>10–12</sup> (in mammals) (Supplementary Fig. 1). Pump activity is stimulated by binding of calcium-loaded calmodulin ( $\text{Ca}^{2+}$ -CaM) to the regulatory domain, thereby inducing a conformational change that displaces the autoinhibitory domain from the pump core structure<sup>13,14</sup>. Calmodulin (CaM) substantially increases both  $\text{Ca}^{2+}$  affinity and pump rate in PMCA<sup>1</sup>. To investigate the mechanism of CaM-mediated PMCA regulation, we have determined the structure of an intact regulatory domain (residues 40–95) of the *Arabidopsis thaliana* PMCA (we denote this domain Aca8R) in a homologous complex with *A. thaliana* Cam7 and characterized it *in vivo* and *in vitro*.

The crystal structure of this complex, determined at a resolution of 1.95 Å, shows an overall dumbbell shape and reveals an unexpected 2:1 stoichiometry (Fig. 1a and Supplementary Table 1): Aca8R forms a 56-residue-long  $\alpha$ -helix with two  $\text{Ca}^{2+}$ -Cam7 molecules bound at two distinct CaM-binding sites within the autoinhibitory domain in a

pseudo-symmetrically ‘inverted’ arrangement. Given this structure, we denote the complex (Cam7)<sub>2</sub>-Aca8R. The two binding sites are separated in space by eight residues with no interaction between the two CaM molecules. Although the first binding site (CaMBS1) had been previously mapped by mutational studies<sup>15</sup>, the second binding site (CaMBS2) was unknown and unexpected.

Both sites show typical structural characteristics of CaM-target recognition<sup>16</sup>. The hydrophobic anchor points are Trp 47 and Phe 60 in CaMBS1 and Ile 79 and Phe 92 in CaMBS2. Each anchor residue is docked in a hydrophobic cage formed in each lobe of Cam7 (Fig. 1b–d and Supplementary Figs 2 and 3). In both of the binding sites the anchor points show a 1–14 spacing, whereas in CaM complexes of human PMCA4b<sup>17</sup> and plant BCA1<sup>18</sup> a 1–18 spacing of anchor residues has been observed. A superimposition of the two bound CaM molecules reveals that the molecule bound to CaMBS1 has a slightly more closed conformation. The long  $\alpha$ -helix formed by the regulatory domain of Aca8 shows a minor bending in CaMBS1.

Small-angle X-ray scattering (SAXS) data of the purified Cam7–Aca8R complex in solution agree with the crystal structure of the 2:1 complex. The distance distribution function shows two separated peaks indicating the presence of two subdomains (Supplementary Fig. 4), and the *ab initio* SAXS model superimposes with the crystal structure (Supplementary Fig. 4). In contrast, a putative 1:1 Cam7–Aca8R binding model does not fit the experimental SAXS data, indicating that the 2:1 (Cam7)<sub>2</sub>-Aca8R complex is indeed the favoured, stable complex in solution.

Using isothermal titration calorimetry (ITC), we measured CaM binding to the isolated binding sites as well as to a construct containing the entire autoinhibitory/regulatory domain of the protein Aca8. Cam7 binds tightly to peptides corresponding to CaMBS1 (dissociation constant,  $K_d = 13$  nM) and CaMBS2 ( $K_d = 0.5$   $\mu$ M) of Aca8 (Fig. 1e, f and Supplementary Table 2). When measuring CaM binding to a construct comprising the entire autoinhibitory/regulatory domain (Aca8(40–126)), biphasic binding to two CaM-binding sites was observed with affinities similar to those of binding to individual peptides (Fig. 1g), whereas apo-CaM (stripped using EDTA) did not bind to any construct (data not shown). This indicates that the regulatory domain of Aca8 indeed contains two independent sites that bind  $\text{Ca}^{2+}$ -CaM with different, but physiologically relevant, affinities.

We performed functional complementation assays using a  $\text{Ca}^{2+}$ -ATPase-deficient yeast strain (K616<sup>19,20</sup>). This allowed us to investigate the autoinhibitory function of the R domain from PMCA gain-of-function mutations, because heterologous expression of a constitutively active  $\text{Ca}^{2+}$  pump in the endoplasmic reticulum of the yeast is required to maintain internal calcium stores on growth in EGTA-containing medium (see Supplementary Information for a detailed account of this model). Indeed, without galactose-driven expression

<sup>1</sup>Centre for Membrane Pumps in Cells and Disease — PUMPKIN, Aarhus University, Gustav Wieds Vej 10c, DK-8000 Aarhus C, Denmark. <sup>2</sup>Department of Molecular Biology and Genetics, Aarhus University, Gustav Wieds Vej 10c, DK-8000 Aarhus C, Denmark. <sup>3</sup>Department of Plant Biology and Biotechnology, University of Copenhagen, Thorvaldsensvej 40, DK-1871 Frederiksberg C, Denmark. <sup>4</sup>MRC Laboratory of Molecular Biology, Hills Road, Cambridge CB2 0QH, UK. <sup>5</sup>Bioinformatics Research Centre, Aarhus University, CF Møllers Allé 8, DK-8000 Aarhus C, Denmark. <sup>6</sup>Department of Mathematical Sciences, University of Copenhagen, Universitetsparken 5, DK-2100 Copenhagen, Denmark. †Present address: Centre for Molecular Medicine Norway, Nordic EMBL Partnership, University of Oslo, PO Box 1125, Blindern, N-0318 Oslo, Norway.

\*These authors contributed equally to this work.

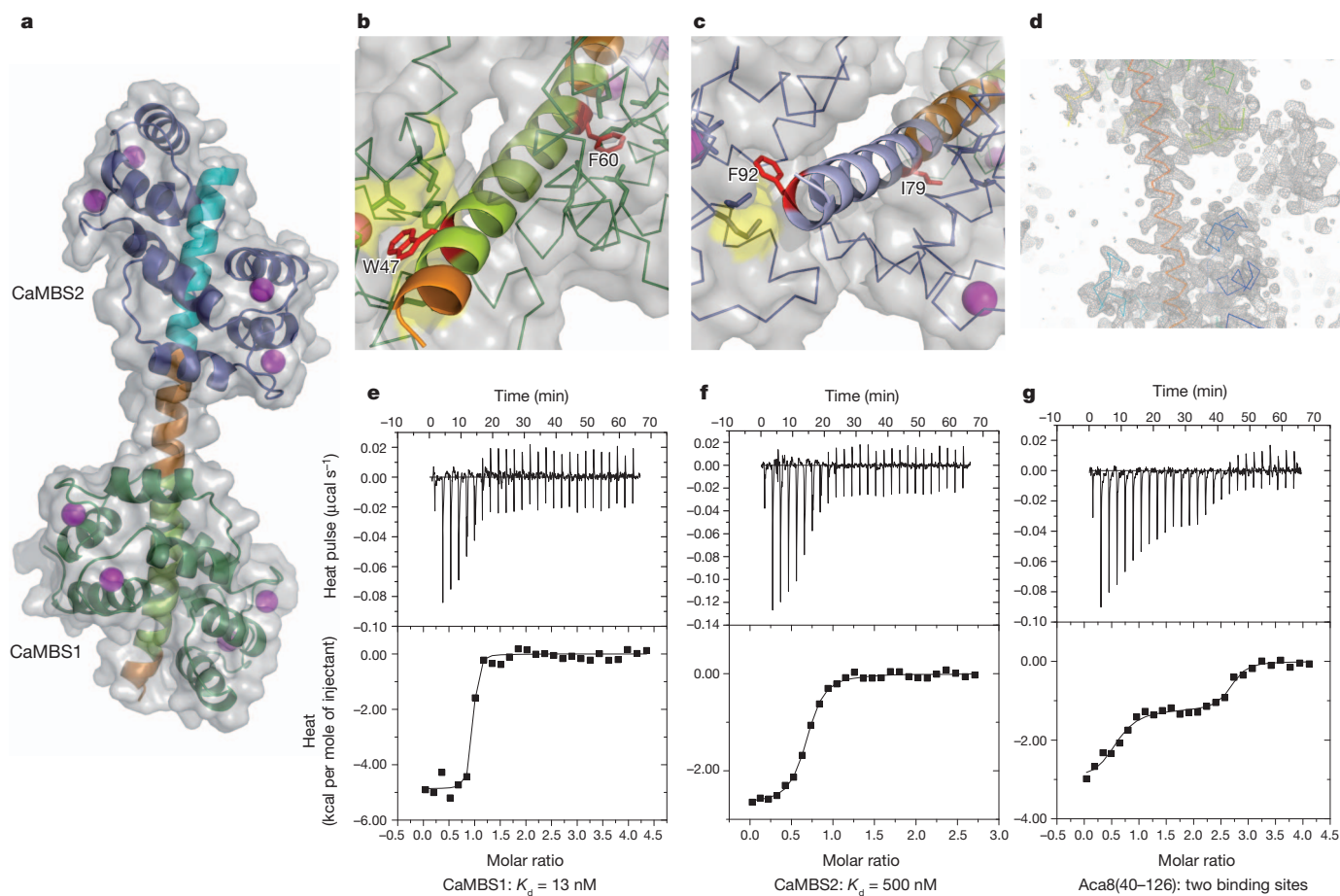


**Figure 1** | Overall structure of the *A. thaliana* (Cam7)<sub>2</sub>-Aca8R complex.

**a**, Representation with CaM molecules in dark green (CaMBS1) and dark blue (CaMBS2), and Aca8R in orange, light green (CaMBS1) and cyan (CaMBS2). Ca<sup>2+</sup> is shown in magenta. **b, c**, Detailed view of hydrophobic anchor residues involved in CaM-binding in CaMBS1 (**b**) and CaMBS2 (**c**). Cam7 is shown as ribbon. Residues in Cam7 that are within van der Waals bonding distance of the Aca8R anchor residues (red sticks) are shown as sticks with yellow surfaces. **d**, Electron density illustrating the extended  $\alpha$ -helix (containing both

CaM-binding sites) formed by the autoinhibitory region. **e–g**, Binding of Cam7 to the autoinhibitory domain of Aca8, examined by ITC. Typical ITC data are shown for the binding of Cam7 to 24-mer peptides corresponding to CaMBS1 (**e**) and CaMBS2 (**f**) of Aca8 and to Aca8(40–126) containing both CaM-binding sites (**g**). Upper panels: raw heat pulse data. Lower panels: integrated heat pulses, normalized per mole of injectant, giving differential binding curves that are adequately described by a one-site (**e** and **f**) or two-site (**g**) binding model with  $K_d = 13$  nM for CaMBS1 and  $K_d = 500$  nM for CaMBS2.

of Aca8 variants, none of the K616 yeast grows in Ca<sup>2+</sup>-depleted medium (Fig. 2a, SD medium). However, expression of a constitutively active Ca<sup>2+</sup> pump by virtue of truncation of either one or both CaM-binding sites ( $\Delta 74$ Aca8 or  $\Delta 100$ Aca8) complements the lack of endogenous yeast Ca<sup>2+</sup>-ATPases and allows growth in the Ca<sup>2+</sup>-depleted medium (Fig. 2a, SG medium), whereas the wild-type autoinhibited Aca8 does not. Yeasts with anchor-point mutations in Aca8 CaMBS1 (Trp47Ala and Phe60Ala) but not in CaMBS2 (Phe92Ala) show moderate growth, indicating that displacement of CaMBS1 alone generates basal pump activity. The Trp47Ala Phe92Ala double mutant with mutation in both CaM-binding sites shows significantly better growth (Fig. 2a) than the Trp47Ala mutant, indicating further involvement of anchor point Phe92Ala (CaMBS2) in autoinhibition. Expression levels were similar for all Aca8 constructs (Supplementary Fig. 5). The results confirm that both CaM-binding sites contribute to autoinhibition of the pump.

The Ca<sup>2+</sup>-stimulated ATPase activity of wild-type Aca8 further shows that the pump encompasses both a high- and a low-affinity sensor for Ca<sup>2+</sup> (via Ca<sup>2+</sup>-CaM; Fig. 2b). Wild-type Aca8 is inactive (autoinhibited) in the absence of CaM and active in its presence. The  $\Delta 74$ Aca8 truncated form, lacking the high-affinity CaM-binding site, shows basal activity and can be further activated twofold by CaM, whereas the  $\Delta 100$ Aca8 form, which lacks both CaM-binding sites, shows CaM-independent activity (Fig. 2b). Furthermore, the characterization

of the different Aca8 mutants supports the proposal that both CaM-binding sites contribute to autoinhibition as well as to Ca<sup>2+</sup>-CaM-mediated activation of the pump (Fig. 2c).

The presence of two CaM-binding sites is, however, not unique to the *A. thaliana* Aca8 protein. Sequence analysis suggests that both CaM-binding sites are conserved in other *Arabidopsis* Aca isoforms and plant PMCA homologues (Supplementary Fig. 6). Even more surprisingly, our analysis of mammalian PMCA (PMCA1 to PMCA4) sequences indicates that tandem CaM-binding sites are generated through alternative splicing in several variants (Fig. 3). The autoinhibitory domain of mammalian PMCA is C-terminal and subject to tissue- and cell-type-specific alternative splicing<sup>5,21</sup>. PMCA splice variants show not only differences with respect to inhibition and CaM activation but also in response to different Ca<sup>2+</sup> signals<sup>5</sup>, supporting the idea that alternative splicing might be a general mechanism for the fine-tuning of intracellular signalling<sup>22–24</sup>. Binding experiments by ITC using peptides of PMCA splice variants (PMCA1 to PMCA4) confirmed that CaM binds to their second sites with  $K_d$  values in the low-micromolar range (Fig. 3a–d and Supplementary Table 2), indicating that several mammalian PMCA variants also interact with two CaM molecules. The spacing between the CaM-binding sites is comparable to that in Aca8, suggesting a similar 2:1 structural arrangement and a similar mechanism of two-step, Ca<sup>2+</sup>-dependent activation by CaM.

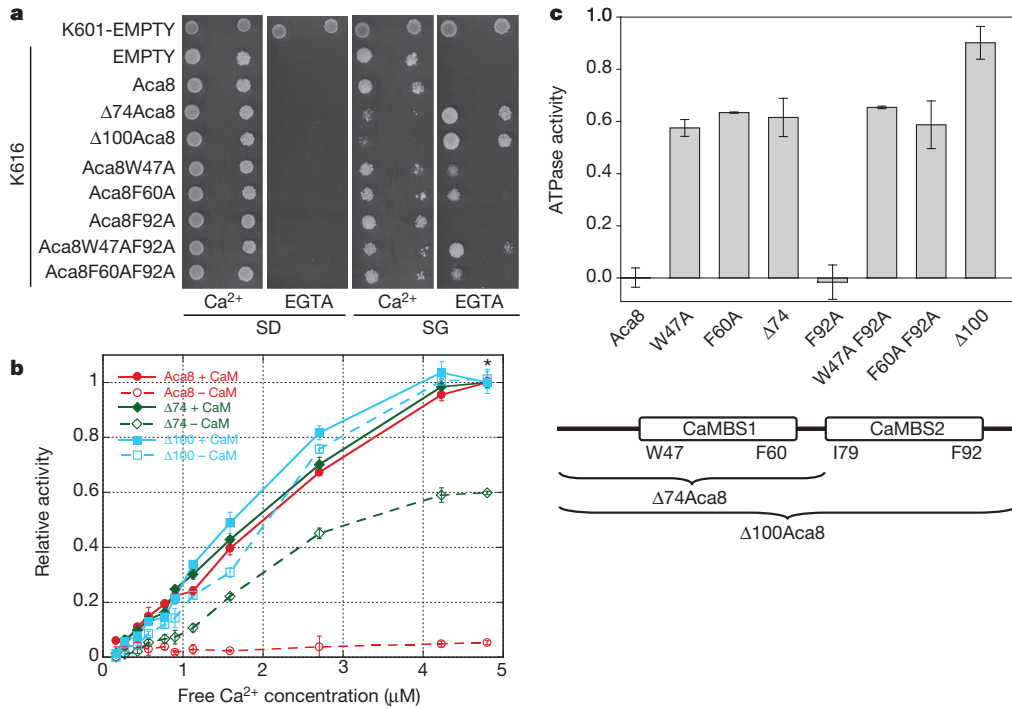


**Figure 2 | Physiological and biochemical characterization of wild-type Aca8 and mutants.** **a**, Functional complementation of the  $\text{Ca}^{2+}$ -ATPase-deficient yeast strain (K616) expressing wild-type and mutants of Aca8. Yeast strains K601 (wild type) and K616 transformed with empty vector are used as positive and negative controls, respectively. K616 transformed with wild-type and mutants of Aca8 regulated by a galactose-inducible promoter are grown on galactose (SG) or glucose (SD) medium supplemented with either 10 mM  $\text{CaCl}_2$  ( $\text{Ca}^{2+}$ ) or 10 mM EGTA. Only deregulated pumps are able to complement the lack of endogenous yeast  $\text{Ca}^{2+}$ -ATPases in  $\text{Ca}^{2+}$ -depleted medium (SG EGTA). **b**,  $\text{Ca}^{2+}$ -stimulated ATPase activity of wild-type Aca8 and truncation variants lacking either CaMBS1 ( $\Delta 74\text{Aca8}$ ) or both CaM-binding sites ( $\Delta 100\text{Aca8}$ ) in the presence or absence of

10  $\mu\text{M}$  Cam7. The asterisk denotes the concentration of free  $\text{Ca}^{2+}$  measured by the  $\text{Ca}^{2+}$ -sensitive dye fura-2 (4.80  $\mu\text{M}$ ), which gave rise to the greatest difference between the activities with and without CaM and was used for normalization (each construct was normalized separately to allow direct comparison of the effect of CaM) and further characterization. The plot shows the results of one of two independent experiments carried out in triplicate. Errors, s.d. **c**, Top: ATPase activity of wild-type and mutant Aca8. The ratio of CaM-independent activity ( $\text{Ca}^{2+}$  with no Cam7) is given relative to the  $\text{Ca}^{2+}$ -CaM-dependent activity ( $\text{Ca}^{2+}$  with 10  $\mu\text{M}$  Cam7). Errors, s.d. (2–4 independent experiments in triplicate). Bottom: schematic of the two CaM-binding sites; the position of anchor point residues and the parts removed in the truncated versions of Aca8 are indicated.

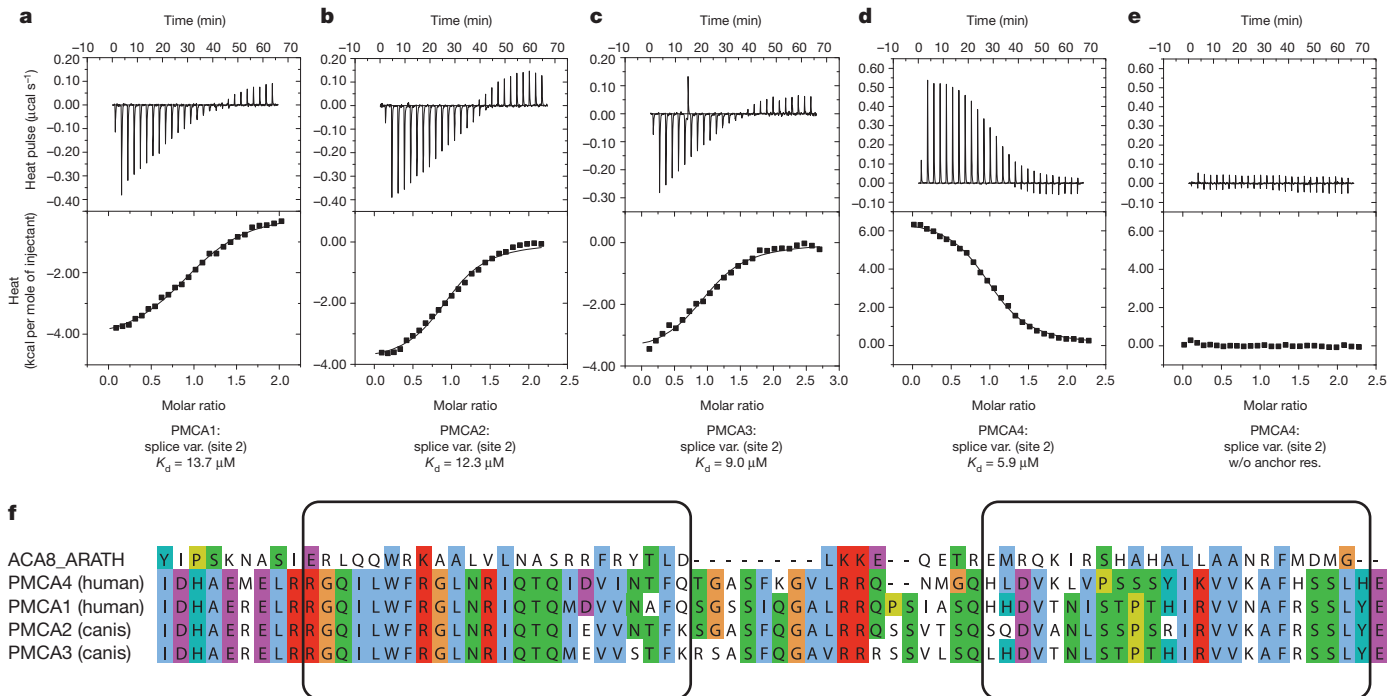


**Figure 3 | Binding of CaM to the putative second CaM-binding site of PMCA splice variants.** **a–d**, Typical ITC data for the binding of mammalian CaM to 24-mer peptides corresponding to splice variants of PMCA1 (**a**), PMCA2 (**b**), PMCA3 (**c**), and PMCA4 (**d**). Upper panels: raw heat pulse data. Lower panels: integrated heat pulses, normalized per mole of injectant, giving differential

binding curves that are adequately described by a one-site binding model. **e**, Control peptide lacking the hydrophobic anchor residues of PMCA4d (Val4Ala, Leu6Ala and Phe19Ala), illustrating that CaM binding is specific. **f**, Alignment of Aca8 and mammalian PMCA splice variants coloured according to the CLUSTAL colouring scheme. The two CaM-binding sites are enclosed with boxes.

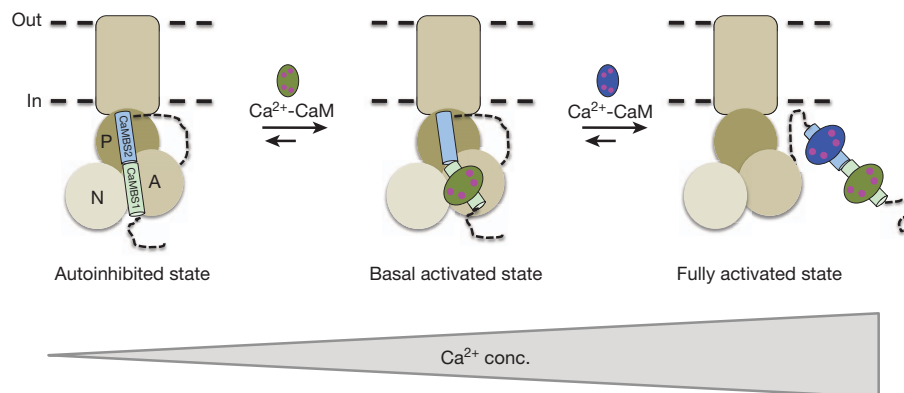


**Figure 4 | Schematic of the proposed two-step,  $\text{Ca}^{2+}$ -mediated CaM-activation mechanism.** With increasing  $\text{Ca}^{2+}$  concentration,  $\text{Ca}^{2+}$ -CaM first binds to and displaces high-affinity CaMBS1 before even higher  $\text{Ca}^{2+}$  concentration leads to displacement of CaMBS2 from the catalytic core,

Using mathematical network modelling of two-binding-site  $\text{Ca}^{2+}$ -CaM activation of PMCA, we find that the pump system is ready for steep activation above a basal  $\text{Ca}^{2+}$  concentration, meaning that the enzyme is inactive below this level and rapidly activates as soon as concentrations exceed it (Supplementary Fig. 7). This gives our results particular physiological relevance, because  $\text{Ca}^{2+}$  activation through just one or no CaM-binding or autoinhibitory site (assuming otherwise identical conditions) is much less abrupt, meaning that a minimal cellular  $\text{Ca}^{2+}$  concentration would be less stable and acceleration of pump activity at increased  $\text{Ca}^{2+}$  levels less pronounced.

By combining structural, physiological and biochemical data with modelling, we also derive a structural model for Aca8 in its autoinhibited state. Aca8 homology models in  $\text{Ca}^{2+}$ -bound (E1) and  $\text{Ca}^{2+}$ -free (E2) conformations reveal the presence of a highly conserved cleft, situated between the A domain and the N and P domains, that is fully exposed in the E2 conformation and buried in the E1 conformation (Supplementary Video 1 and Supplementary Figs 8 and 9). Several acidic residues previously reported to be involved in autoinhibition (Glu 252, Asp 303 and Asp 332) cluster along this region<sup>25</sup> (Supplementary Fig. 9). The N-terminal autoinhibitory domain of Aca8, however, contains several conserved basic residues<sup>15</sup> (Arg 58, Arg 61, Lys 67 and Lys 68), which are of critical importance for autoinhibition and could potentially interact with the acidic residues mentioned above (Supplementary Fig. 8). We suggest that as the  $\text{Ca}^{2+}$  concentration increases,  $\text{Ca}^{2+}$ -CaM first binds to and displaces the high-affinity CaMBS1 in the region between the A and N domains, and that further  $\text{Ca}^{2+}$ -CaM activation leads to displacement of CaMBS2 from the linker regions between the transmembrane domain and the mobile A domain (Fig. 4 and Supplementary Fig. 8). Displacement of CaMBS1 allows free movement of the cytoplasmic domains as required for ion pumping at basal levels, and the additional displacement of CaMBS2 by higher  $\text{Ca}^{2+}$ -CaM concentrations or the presence of acidic phospholipids<sup>26</sup> results in further activity. This model provides a conceptual framework for a bimodular,  $\text{Ca}^{2+}$ -mediated CaM-activation mechanism that allows regulation of intracellular  $\text{Ca}^{2+}$  concentration over a broad range of physiological conditions, ready to respond promptly at increased  $\text{Ca}^{2+}$  levels and setting the basal  $\text{Ca}^{2+}$  level in the cell. Such a mechanism seems to be well suited to the fine-tuning of calcium homeostasis and intracellular signalling in eukaryotes.

## METHODS SUMMARY

Procedures for the expression, purification and crystallization of the (Cam7)<sub>2</sub>-Aca8R complex were similar to those described in ref. 27. The complex was crystallized at 4 °C using sitting-drop vapour diffusion against a reservoir containing 1.9 M  $(\text{NH}_4)_2\text{SO}_4$ , 0.1 M CAPS (pH 10.5) and 0.2 M  $\text{Li}_2\text{SO}_4$ . The crystals have space group  $P4_12_12$  and unit-cell parameters  $a = b = 71.25 \text{ \AA}$ ,  $c = 163.28 \text{ \AA}$  and

allowing free movement of the A domain as required for ion pumping. Actuator (A), nucleotide-binding (N) and phosphorylation (P) domains and the transmembrane region are indicated. Aca8R is shown as cylinder with the CaM-binding site colour-coded as in Fig. 1.

$\alpha = \beta = \gamma = 90^\circ$ . Diffraction data were collected to a resolution limit of 1.95 Å at the ID23-2 beamline of the European Synchrotron Radiation Facility (France). The structure was determined by molecular replacement followed by iterative model building and refinement. The final model yielded a crystallographic *R*-factor of 22.1% and a free *R*-factor of 25.3%. Evaluation of the Ramachandran plot showed all residues except one (99.7%) in allowed regions (97.0% in favoured regions). SAXS data were collected at the X33 beamline at EMBL/DESY (Germany), following standard procedures. Heterologous expression, yeast complementation tests, membrane purification and activity assays of full-length Aca8, N-terminal truncation and single-point-mutation constructs were performed essentially as previously described<sup>15,28</sup>. More detailed methods can be found in Method and Supplementary Information.

**Full Methods** and any associated references are available in the online version of the paper.

Received 2 December 2011; accepted 23 August 2012.

Published online 21 October 2012.

- Clapham, D. E. Calcium signaling. *Cell* **131**, 1047–1058 (2007).
- Carafoli, E. Calcium signaling: a tale for all seasons. *Proc. Natl Acad. Sci. USA* **99**, 1115–1122 (2002).
- Ghosh, A. & Greenberg, M. E. Calcium signaling in neurons: molecular mechanisms and cellular consequences. *Science* **268**, 239–247 (1995).
- Berridge, M. J. Inositol trisphosphate and calcium signalling. *Nature* **361**, 315–325 (1993).
- Strehler, E. E., Filoteo, A. G., Penniston, J. T. & Caride, A. J. Plasma-membrane  $\text{Ca}^{2+}$  pumps: structural diversity as the basis for functional versatility. *Biochem. Soc. Trans.* **35**, 919–922 (2007).
- Brini, M. & Carafoli, E. Calcium pumps in health and disease. *Physiol. Rev.* **89**, 1341–1378 (2009).
- Brini, M. & Carafoli, E. The plasma membrane  $\text{Ca}^{2+}$  ATPase and the plasma membrane sodium calcium exchanger cooperate in the regulation of cell calcium. *Cold Spring Harb. Perspect. Biol.* **3**, 1–15 (2011).
- Axelsen, K. B. & Palmgren, M. G. Evolution of substrate specificities in the P-type ATPase superfamily. *J. Mol. Evol.* **46**, 84–101 (1998).
- Malmström, S., Askerlund, P. & Palmgren, M. G. A calmodulin-stimulated  $\text{Ca}^{2+}$ -ATPase from plant vacuolar membranes with a putative regulatory domain at its N-terminus. *FEBS Lett.* **400**, 324–328 (1997).
- Falchetto, R., Vorherr, T., Brunner, J. & Carafoli, E. The plasma membrane  $\text{Ca}^{2+}$  pump contains a site that interacts with its calmodulin-binding domain. *J. Biol. Chem.* **266**, 2930–2936 (1991).
- Falchetto, R., Vorherr, T. & Carafoli, E. The calmodulin-binding site of the plasma membrane  $\text{Ca}^{2+}$  pump interacts with the transduction domain of the enzyme. *Protein Sci.* **1**, 1613–1621 (1992).
- Bonza, M. C. & Luoni, L. Plant and animal type 2B  $\text{Ca}^{2+}$ -ATPases: evidence for a common auto-inhibitory mechanism. *FEBS Lett.* **584**, 4783–4788 (2010).
- Carafoli, E. Biogenesis: plasma membrane calcium ATPase: 15 years of work on the purified enzyme. *FASEB J.* **8**, 993–1002 (1994).
- Penniston, J. T. & Enyedi, A. Modulation of the plasma membrane  $\text{Ca}^{2+}$  pump. *J. Membr. Biol.* **165**, 101–109 (1998).
- Baekgaard, L., Luoni, L., De Michelis, M. I. & Palmgren, M. G. The plant plasma membrane  $\text{Ca}^{2+}$  pump ACA8 contains overlapping as well as physically separated autoinhibitory and calmodulin-binding domains. *J. Biol. Chem.* **281**, 1058–1065 (2006).
- Hoeflich, K. P. & Ikura, M. Calmodulin in action: diversity in target recognition and activation mechanisms. *Cell* **108**, 739–742 (2002).

17. Juranic, N. *et al.* Calmodulin wraps around its binding domain in the plasma membrane  $\text{Ca}^{2+}$  pump anchored by a novel 18–1 motif. *J. Biol. Chem.* **285**, 4015–4024 (2010).
18. Ishida, H. & Vogel, H. J. The solution structure of a plant calmodulin and the CaM-binding domain of the vacuolar calcium-ATPase BCA1 reveals a new binding and activation mechanism. *J. Biol. Chem.* **285**, 38502–38510 (2010).
19. Cunningham, K. W. & Fink, G. R. Calcineurin-dependent growth control in *Saccharomyces cerevisiae* mutants lacking PMC1, a homolog of plasma membrane  $\text{Ca}^{2+}$  ATPases. *J. Cell Biol.* **124**, 351–363 (1994).
20. Durr, G. *et al.* The medial-Golgi ion pump Pmr1 supplies the yeast secretory pathway with  $\text{Ca}^{2+}$  and  $\text{Mn}^{2+}$  required for glycosylation, sorting, and endoplasmic reticulum-associated protein degradation. *Mol. Biol. Cell* **9**, 1149–1162 (1998).
21. Strehler, E. E. & Zacharias, D. A. Role of alternative splicing in generating isoform diversity among plasma membrane calcium pumps. *Physiol. Rev.* **81**, 21–50 (2001).
22. Enyedi, A. *et al.* The  $\text{Ca}^{2+}$  affinity of the plasma membrane  $\text{Ca}^{2+}$  pump is controlled by alternative splicing. *J. Biol. Chem.* **269**, 41–43 (1994).
23. Namba, T. *et al.* Alternative splicing of C-terminal tail of prostaglandin E receptor subtype EP3 determines G-protein specificity. *Nature* **365**, 166–170 (1993).
24. Spengler, D. *et al.* Differential signal transduction by five splice variants of the PACAP receptor. *Nature* **365**, 170–175 (1993).
25. Fusca, T. *et al.* Single point mutations in the small cytoplasmic loop of ACA8, a plasma membrane  $\text{Ca}^{2+}$ -ATPase of *Arabidopsis thaliana*, generate partially deregulated pumps. *J. Biol. Chem.* **284**, 30881–30888 (2009).
26. Meneghelli, S., Fusca, T., Luoni, L. & De Michelis, M. I. Dual mechanism of activation of plant plasma membrane  $\text{Ca}^{2+}$ -ATPase by acidic phospholipids: Evidence for a phospholipid binding site which overlaps with the calmodulin-binding site. *Mol. Membr. Biol.* **25**, 539–546 (2008).
27. Tidow, H., Hein, K. L., Baekgaard, L., Palmgren, M. G. & Nissen, P. Expression, purification, crystallization and preliminary X-ray analysis of calmodulin in complex with the regulatory domain of the plasma-membrane  $\text{Ca}^{2+}$ -ATPase ACA8. *Acta Crystallogr. F* **66**, 361–363 (2010).
28. Schiott, M. *et al.* A plant plasma membrane  $\text{Ca}^{2+}$  pump is required for normal pollen tube growth and fertilization. *Proc. Natl Acad. Sci. USA* **101**, 9502–9507 (2004).

**Supplementary Information** is available in the online version of the paper.

**Acknowledgements** We thank members of the Nissen and Palmgren labs for discussions, and P. Gourdon for help with data collection. We thank the staff at beamlines ID23-2 at the European Radiation Synchrotron Facility, France; PX3 at the Swiss Light Source, Paul Scherrer Institute, Switzerland; and X33 at EMBL/DESY, Germany. We are grateful to K. Nagai for a plasmid expressing mammalian CaM. Support from the European Community-Research Infrastructure Action under the FP7 is acknowledged for access to EMBL/DESY. H.T. is a Junior Research Fellow at Trinity College, Cambridge, and was supported by an EMBO Long-Term Fellowship, a Marie-Curie Intra-European Fellowship and an HFSP Long-Term Fellowship. P.N. was supported by an ERC advanced grant (BIOMEMOS).

**Author Contributions** H.T. designed and initiated the project, designed the expression constructs and developed the co-expression strategy, initially assisted by K.L.H. Protein purification, crystallization, structure determination and refinement, and the overall analysis of the results, was performed by H.T. L.R.P. performed biochemical and genetic analyses of Aca8 and derived mutants, developed methods for measuring calcium concentrations *in vitro*, and analysed biochemical and yeast complementation assays, supervised by M.G.P. A.A. performed bioinformatics sequence analysis, homology modelling and docking experiments. M.K. performed mathematical modelling, supervised by C.W. P.N. designed and supervised the project, and analysed results. H.T., L.R.P., A.A., M.G.P. and P.N. wrote the paper, and all authors commented on the paper.

**Author Information** Atomic coordinates and structure factors for the crystal structure of (Cam7)<sub>2</sub>-Aca8R have been deposited with the Protein Data Bank under accession code 4AQR. Reprints and permissions information is available at [www.nature.com/reprints](http://www.nature.com/reprints). The authors declare no competing financial interests. Readers are welcome to comment on the online version of the paper. Correspondence and requests for materials should be addressed to M.G.P. ([palmgren@life.ku.dk](mailto:palmgren@life.ku.dk)) or P.N. ([pn@mb.au.dk](mailto:pn@mb.au.dk)).

## METHODS

**Purification and crystallization of (Cam7)<sub>2</sub>-Aca8R.** Purification of the complex and initial crystallization was performed as previously described<sup>27</sup>. In brief, Aca8(40–95) and Cam7 (both from *A. thaliana*) were co-expressed in *Escherichia coli* C41 cells<sup>29</sup> and purified using standard His-tag purification protocols followed by TEV protease digestion, a second Ni-affinity chromatography step to separate a fusion protein tag and a final gel-filtration step. Initial crystals were obtained using the vapour diffusion technique in sitting drops prepared by mixing 1.5 µl of (Cam7)<sub>2</sub>-Aca8R solution (16 mg ml<sup>-1</sup>) with 1 µl of reservoir solution, and equilibrated against reservoir solution containing 2.0 M (NH<sub>4</sub>)<sub>2</sub>SO<sub>4</sub>, 0.1 M CAPS (pH 10.5) and 0.2 M Li<sub>2</sub>SO<sub>4</sub> (final pH 8.2) at room temperature (293 K). These crystals belonged to space group C2 and diffracted to a resolution of 3.0 Å (ref. 27). Better-diffracting crystals belonging to a different space group (P<sub>4</sub>2<sub>1</sub>2) were obtained at 4 °C under slightly modified conditions: 1 µl of (Cam7)<sub>2</sub>-Aca8R solution (16 mg ml<sup>-1</sup>) was mixed with 1 µl of reservoir solution and equilibrated against reservoir solution containing 1.9 M (NH<sub>4</sub>)<sub>2</sub>SO<sub>4</sub>, 0.1 M CAPS (pH 10.5) and 0.2 M Li<sub>2</sub>SO<sub>4</sub> at 4 °C (277 K). Crystals appeared after several months, grew to maximum dimensions of 0.7 mm × 0.35 mm × 0.2 mm within weeks (Supplementary Fig. 10) and proved to be superior to the room-temperature crystal with respect to diffraction properties. Crystals were mounted and flash-cooled in liquid nitrogen without additional cryoprotection.

**Characterization of CaM-binding sites using complementation tests and activity assays.** Cam7 from *A. thaliana* and mammalian CaM alone were expressed in *E. coli* C41 and purified using standard His-tag purification protocols. Heterologous expression, yeast complementation tests, membrane purification and activity assays of full-length Aca8, N-terminal truncation and single-point-mutation constructs were performed essentially as previously described<sup>15,28</sup>. The yeast strain K616 lacks the regulatory subunit B (Cnb1) of calcineurin in addition to the two Ca<sup>2+</sup>-ATPases (Pmc1 and Pmr1). Under normal conditions, calcineurin inhibits the low-affinity vacuolar Ca<sup>2+</sup>/H<sup>+</sup> antiporter Vcx1. Vcx1 is the only transporter that can fill up the vacuolar Ca<sup>2+</sup> store in the mutant lacking the two Ca<sup>2+</sup>-ATPases. At high Ca<sup>2+</sup> concentration in the cytosol, Vcx1 transports Ca<sup>2+</sup> into the vacuole. Therefore, to get a viable yeast strain, the *cnb1* mutation is required. The mutation of calcineurin activates the antiporter, which then removes Ca<sup>2+</sup> from the cytosol. At low Ca<sup>2+</sup> concentration, the K616 strain needs an active high-affinity transporter (Ca<sup>2+</sup>-ATPase) to remove Ca<sup>2+</sup> from the cytosol; that is, complementation requires a constitutively active Ca<sup>2+</sup> pump in the endoplasmic reticulum/Golgi apparatus apparently to scavenge trace Ca<sup>2+</sup> for proper functioning of the secretory pathway. It has previously been shown that only expression of active Ca<sup>2+</sup>-ATPases can rescue the growth defect in Ca<sup>2+</sup>-depleted medium<sup>15</sup>. The growth rate of the mutant in Ca<sup>2+</sup>-depleted medium thus provides an *in vivo* assay for functional characterization of overexpressed recombinant Ca<sup>2+</sup> pumps from heterologous sources.

The expression level of Aca8 and mutants in yeast microsomal membranes (20 µg) were determined by SDS-polyacrylamide gel electrophoresis. The biochemical characterization was carried out on microsomal membranes (5 µg). ATPase activity was determined with and without 10 µM Cam7 by varying the free Ca<sup>2+</sup> concentration. The free Ca<sup>2+</sup> concentrations were determined using the Ca<sup>2+</sup>-sensitive dye fura-2 (ref. 30). Calibration curves were generated using the Calcium Calibration Buffer Kit #1 (zero and 10 mM CaEGTA) and fura-2 pentapotassium salt (Invitrogen/Molecular Probes). Each buffer and ATPase assay sample (prepared as for the ATPase activity assay) was supplemented with 1 µM fura-2. For each calibration buffer and test sample, excitation scans were generated between wavelengths 250 and 450 nm (slit, 5 nm) while detecting the emission at wavelength 510 nm (slit, 5 nm) essentially as described in the provided protocol from Invitrogen. The HORIBA Jobin Yone FluoroMax-4 spectrofluorometer and the software FLUORESSANCE were used for the measurements. For the final calculations, fluorescence at 380 nm (F380) was used. The free Ca<sup>2+</sup> concentration in the calibration kit buffer was calculated using the specific K<sub>d</sub> (EGTA) values at pH 7.3 (30 °C). The addition of Cam7 in the absence of Ca<sup>2+</sup> did not result in any change in ATPase activity. Activity without Ca<sup>2+</sup> and Cam7 were subtracted from those with Ca<sup>2+</sup> and with and without Cam7 to give the measured Ca<sup>2+</sup>-ATPase activity.

**Data collection and X-ray diffraction analysis.** Diffraction data were collected to a resolution limit of 1.95 Å. Two full data sets containing 200 oscillation images each with an interval of 1° were collected using the same crystal at a wavelength of 0.9464 Å at the ID23-2 beamline of the European Synchrotron Radiation Facility (France). Exposure times and crystal-to-detector distances were respectively 0.4 s and 472 mm (set one) and 0.5 s and 245 mm (set two). Low-resolution and high-resolution data sets were merged using XSCALE<sup>31</sup>.

Reflections were indexed and scaled with XDS<sup>31</sup>. The crystals belonged to the tetragonal space group P<sub>4</sub>2<sub>1</sub>2 and had unit-cell parameters  $a = b = 71.25$  Å,

$c = 163.28$  Å and  $\alpha = \beta = \gamma = 90^\circ$ . A summary of the data statistics is given in Supplementary Table 1.

**Structure determination.** The structure was solved by molecular replacement using PHASER<sup>32</sup> with a systematic combination of search models (derived from various CaM complexes) and search parameters. An initial molecular replacement solution contained two molecules of CaM N-terminal domain and one molecule of CaM C-terminal domain and revealed clear extra density that could be unambiguously assigned to Aca8R. Subsequent rounds of manual building using COOT<sup>33</sup> and refinement using PHENIX.REFINE<sup>34</sup> allowed placement of the second CaM C-terminal domain and led to almost complete model building (five residues (76–80) in a flexible linker connecting Cam7 lobes bound to CaMBS2 could not be traced). The final model yielded a crystallographic R-factor of 22.1% and a free R-factor of 25.3%. The model was validated using MOLPROBITY<sup>35,36</sup>. Evaluation of the Ramachandran plot showed all residues except one (99.7% in allowed regions (97.0% in favoured regions), with Ser 82 situated in the flexible loop connecting the N- and C-terminal lobes of Cam7 (CaMBS1) as the single outlier. All figures were prepared using PYMOL<sup>37</sup>. The data are deposited in the Protein Data Bank.

**SAXS — data collection and *ab initio* modelling.** SAXS data were collected at the X33 beamline at EMBL/DESY (Germany), following standard procedures. Repetitive data collection on the same sample was performed and no radiation damage was detected. Samples of (Cam7)<sub>2</sub>-Aca8R solution were prepared in concentrations ranging from 4.5 to 9.0 mg ml<sup>-1</sup> in a buffer containing 40 mM Tris/HCl (pH 7.4), 150 mM NaCl, 5 mM β-mercaptoethanol and 5 mM CaCl<sub>2</sub>. All SAXS data were analysed using the package ATSAS<sup>38</sup>. Raw data were processed using PRIMUS<sup>39</sup>. The radius of gyration ( $R_g$ ) was evaluated using the Guinier approximation ( $I(s) = I(0)\exp(-s^2R_g^2/3)$  for  $sR_g < 1.3$ , where  $I$  denotes intensity and  $s$  denotes momentum transfer) and also from the entire scattering curve with the program GNOM<sup>40</sup>; the latter also provided the distance distribution function,  $p(r)$ , and the maximum dimension,  $D_{max}$ . The masses of the solutes were evaluated by comparison of the forward scattering intensity with that from a BSA reference solution (mass, 66 kDa).

Low-resolution SAXS models were obtained using the *ab initio* simulated annealing program DAMMIN<sup>41</sup>, which generates models consisting of dummy atoms to fit the experimental data  $I_{exp}(s)$  by minimizing the discrepancy

$$\chi^2 = \frac{1}{N-1} \sum_j \left( \frac{I_{exp}(s_j) - cI_{calc}(s_j)}{\sigma(s_j)} \right)^2$$

where  $N$  is the number of experimental points,  $c$  is a scaling factor, and  $I_{calc}(s_j)$  and  $\sigma(s_j)$  are the calculated intensity and the experimental error at the momentum transfer  $s_j$ , respectively. Superimposition of low-resolution dummy atom models was performed using SUPCOMB<sup>42</sup>.

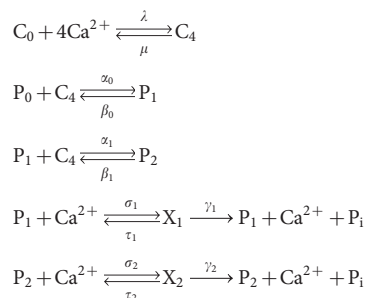
**Isothermal titration calorimetry.** The thermodynamic parameters were determined using an isothermal titration calorimeter (MicroCal ITC<sub>200</sub>, GE Healthcare) at 15 °C in a buffer containing 40 mM Tris/HCl (pH 7.4), 150 mM NaCl, 5 mM β-mercaptoethanol, 5 mM CaCl<sub>2</sub>. For binding of Cam7 to Aca8(40–126) 400 µM Cam7 was titrated into the sample cell containing 20 µM Aca8(40–126). For binding of Cam7 to peptides corresponding to Aca8 CaMBS1 (residues 42–65) and Aca8 CaMBS2 (residues 74–97) typically 150–400 µM of the peptide was titrated into the sample cell containing 7–40 µM Cam7. Reverse titration yielded identical thermodynamic parameters. For binding of mammalian CaM to peptides corresponding to the putative second CaM-binding site of mammalian PMCA1, PMCA2, PMCA3 and PMCA4 splice variants typically 0.6–1.2 mM CaM was titrated into the sample cell containing 50–100 µM peptide. Injection steps were 1.5 µl (first injection, 0.3 µl) with 150-s spacing. Baseline corrections were performed by titrating protein or peptide into sample buffer and sample buffer into protein or peptide. Further data evaluation (Supplementary Table 2) was done using the MicroCal ORIGIN program. Peptides were purchased from GL Biochem (China; HPLC purified, >90% purity).

The peptide sequences were as follows: Aca8-CaMBS1: ERLQQWRKA ALVLNASRRFRYTLTD; Aca8-CaMBS2: EMRQKIRSHAHALLAANRFMDMGR; PMCA1-CaMBS2: HHDVTNISTPTHIRVVNAFRSSLY; PMCA2-CaMBS2: SQD VANLSSPSRIRVVKAFRSSL; PMCA3-CaMBS2: LHDVTNLSPTPTHIRVVKAFRSSLY; PMCA4-CaMBS2: HLDVKLVPSSSYKVVKAHSSSLH; PMCA4-CaMBS2-minus-anchor: HLDAKAVPSSSYKVVKAHSSSLH.

**Bioinformatics analysis and homology modelling.** Multiple sequence alignments were produced using CLUSTAL W<sup>43</sup>. A sequence motif was generated using WEBLOGO<sup>44</sup>. Homology models of Aca8 in the E1 and E2 conformations were computed with MODELLER<sup>45</sup> using the SERCA structures (Protein Data Bank IDs, 3N5K and 3N8G) as templates and a manually optimized alignment as input. Conservation scores were calculated with CONSURF<sup>46</sup>. Docking of the autoinhibitory N terminus onto the Aca8 homology model was performed with HADDOCK<sup>47,48</sup>

using residues previously observed to be involved in autoinhibition<sup>15,25</sup> (Arg 58, Arg 61, Lys 67, Lys 68, Glu 252, Asp 303 and Asp332) as restraints.

**Mathematical modelling.** We denote free CaM by  $C_0$  and CaM in complex with four  $Ca^{2+}$  ions by  $C_4$ . The autoinhibited wild-type pump is denoted  $P_0$ , whereas  $P_1$  and  $P_2$  denote the pumps with one and, respectively, two CaM-binding sites occupied by  $C_4$  ( $X_1$  and  $X_2$  in the  $Ca^{2+}$ -bound state). Finally,  $P_i$  denotes inorganic phosphorus. The wild-type model is represented by the following set of reactions:



Assuming mass-action kinetics, the reactions give rise to a set of polynomial differential equations. Supplementary Fig. 7 shows a typical output obtained using the reaction rates  $\lambda = 10$ ,  $\mu = 5$ ,  $\alpha_0 = 10$ ,  $\beta_0 = 0.1$ ,  $\alpha_1 = 1$ ,  $\beta_1 = 0.25$ ,  $\sigma_1 = 1$ ,  $\tau_1 = 0.001$ ,  $\gamma_1 = 0.01$ ,  $\sigma_2 = 2$ ,  $\tau_2 = 0.001$  and  $\gamma_2 = 0.1$  and with total amount of CaM equal to 10 and the total amount of PMCA equal to 1. For varying total amounts of  $Ca^{2+}$ , the steady-state concentrations are obtained from numerical simulation of the system of differential equations using MATHEMATICA. The steady-state production rate of inorganic phosphorus

$$\frac{d[P_i]}{dt} = \gamma_1[X_1] + \gamma_2[X_2]$$

where square brackets denote concentration, is used as a measure of pump activity and plotted as a function of the steady-state concentration of free calcium. The  $\Delta$ CaMBS1 and  $\Delta$ CaMBS1+2 models are derived from the wild-type model by leaving out  $P_0$  and, respectively,  $P_0$  and  $P_1$  as well as all reactions in which the omitted pump or pumps participate. All simulations were started with  $[Ca^{2+}] = Ca^{2+}_{tot}$  and  $[C_0] = C_{tot}$  and with all PMCAs in the state with no CaM bound. That is, in states  $P_0$ ,  $P_1$  and  $P_2$  for wild-type,  $\Delta$ CaMBS1 and  $\Delta$ CaMBS1+2, respectively.

We note that the models are nested: all parameters in the  $\Delta$ CaMBS1+2 and  $\Delta$ CaMBS1 models are also parameters in the  $\Delta$ CaMBS1 and, respectively, wild-type models. Simulations were made assuming that  $\alpha_0 > \alpha_1$  and  $\sigma_2 > \sigma_1$ , meaning

that the binding affinity of CaM to CaMBS1 was higher than that of CaM to CaMBS2 and that the activity of  $P_2$  was higher than that of  $P_1$ , respectively.

29. Miroux, B. & Walker, J. E. Over-production of proteins in Escherichia coli: mutant hosts that allow synthesis of some membrane proteins and globular proteins at high levels. *J. Mol. Biol.* **260**, 289–298 (1996).
30. Gryniewicz, G., Poenie, M. & Tsien, R. Y. A new generation of  $Ca^{2+}$  indicators with greatly improved fluorescence properties. *J. Biol. Chem.* **260**, 3440–3450 (1985).
31. Kabsch, W. XDS. *Acta Crystallogr. D* **66**, 125–132 (2010).
32. McCoy, A. J. *et al.* Phaser crystallographic software. *J. Appl. Crystallogr.* **40**, 658–674 (2007).
33. Emsley, P., Lohkamp, B., Scott, W. G. & Cowtan, K. Features and development of Coot. *Acta Crystallogr. D* **66**, 486–501 (2010).
34. Afonine, P. V., Grosse-Kunstleve, R. W. & Adams, P. D. The Phenix refinement framework. *CCP4 Newsletter* **42**, 8 (2005).
35. Chen, V. B. *et al.* MolProbity: all-atom structure validation for macromolecular crystallography. *Acta Crystallogr. D* **66**, 12–21 (2010).
36. Davis, I. W. *et al.* MolProbity: all-atom contacts and structure validation for proteins and nucleic acids. *Nucleic Acids Res.* **35**, W375–W383 (2007).
37. DeLano, W. L. The PyMOL Molecular Graphics System. <http://www.pymol.org> (2002).
38. Konarev, P. V., Petoukhov, M. V., Volkov, V. V. & Svergun, D. I. ATSAS 2.1, a program package for small-angle scattering data analysis. *J. Appl. Crystallogr.* **39**, 277–286 (2006).
39. Konarev, P. V., Volkov, V. V., Sokolova, A. V., Koch, M. H. J. & Svergun, D. I. PRIMUS: a Windows PC-based system for small-angle scattering data analysis. *J. Appl. Crystallogr.* **36**, 1277–1282 (2003).
40. Svergun, D. I. Determination of the regularization parameter in indirect-transform methods using perceptual criteria. *J. Appl. Crystallogr.* **25**, 495–503 (1992).
41. Svergun, D. I. Restoring low resolution structure of biological macromolecules from solution scattering using simulated annealing. *Biophys. J.* **76**, 2879–2886 (1999).
42. Kozin, M. B. & Svergun, D. I. Automated matching of high- and low-resolution structural models. *J. Appl. Crystallogr.* **34**, 33–41 (2001).
43. Thompson, J. D., Higgins, D. G. & Gibson, T. J. CLUSTAL W: improving the sensitivity of progressive multiple sequence alignment through sequence weighting, position-specific gap penalties and weight matrix choice. *Nucleic Acids Res.* **22**, 4673–4680 (1994).
44. Crooks, G. E., Hon, G., Chandonia, J. M. & Brenner, S. E. WebLogo: a sequence logo generator. *Genome Res.* **14**, 1188–1190 (2004).
45. Sali, A. & Blundell, T. L. Comparative protein modelling by satisfaction of spatial restraints. *J. Mol. Biol.* **234**, 779–815 (1993).
46. Glaser, F. *et al.* ConSurf: identification of functional regions in proteins by surface-mapping of phylogenetic information. *Bioinformatics* **19**, 163–164 (2003).
47. Dominguez, C., Boelens, R. & Bonvin, A. M. HADDOCK: a protein-protein docking approach based on biochemical or biophysical information. *J. Am. Chem. Soc.* **125**, 1731–1737 (2003).
48. de Vries, S. J. *et al.* HADDOCK versus HADDOCK: new features and performance of HADDOCK2.0 on the CAPRI targets. *Proteins* **69**, 726–733 (2007).